

PCCP

Accepted Manuscript



This is an *Accepted Manuscript*, which has been through the Royal Society of Chemistry peer review process and has been accepted for publication.

Accepted Manuscripts are published online shortly after acceptance, before technical editing, formatting and proof reading. Using this free service, authors can make their results available to the community, in citable form, before we publish the edited article. We will replace this *Accepted Manuscript* with the edited and formatted *Advance Article* as soon as it is available.

You can find more information about *Accepted Manuscripts* in the [Information for Authors](#).

Please note that technical editing may introduce minor changes to the text and/or graphics, which may alter content. The journal's standard [Terms & Conditions](#) and the [Ethical guidelines](#) still apply. In no event shall the Royal Society of Chemistry be held responsible for any errors or omissions in this *Accepted Manuscript* or any consequences arising from the use of any information it contains.

Cite this: DOI: 10.1039/c0xx00000x

ARTICLE TYPE

www.rsc.org/xxxxxx

Gold Atomic Clusters Extracting the Valence Electrons to Shield the Carbon Monoxide Passivation on Near Monolayers Core-Shell Nanocatalysts in Methanol Oxidation Reactions

Tsan-Yao Chen,^{*a,b} Hong Dao Li,^c Guo-Wei Lee,^c Po-Chun Huang,^a Po-Wei Yang,^a Yu-Ting Liu,^d Yen-Fa Liao,^e Horng-Tay Jeng^c, Deng-Sung Lin^c, and Tsang-Lang-Lin^a

Received (in XXX, XXX) Xth XXXXXXXXX 20XX, Accepted Xth XXXXXXXXX 20XX

DOI: 10.1039/b000000x

Atomic scale gold clusters were intercalated at the inter-facet corner sites of Pt shell Ru core nanocatalysts with near monolayers shell thickness. We demonstrated that these unique clusters could serve as valence electron drain at the kink region of core-shell heterojunction. As complimentary revealed by density functional theory calculation and valence band spectra, these Au clusters extract the core level electron to the valence band. It prevents the protonation corrosion and enhances the CO tolerance by enriching the electronegativity at the NCs outmost surface during methanol oxidation reaction (MOR). In this circumstance, the retained current density of Pt shell Ru core NCs is doubled in a long-term (2 hours) MOR at fix voltage (0.5 volt vs. SCE) by intercalating these sub-nanometer gold rivets. Such novel structure confinement provides possible strategy for developing the high power and stability direct methanol fuel cell (DMFC) modules.

Introduction

The structural and chemical stability of electrocatalyst in long-term methanol oxidation reaction (MOR) is the dominate factor in developing the durable direct-methanol fuel cells (DMFCs) anode with high performance. From heterogeneous interface standpoint, this target can be achieved by growing the nanocatalysts (NCs) with highly stressed intra-particle heterojunction confinements. The binary and ternary metallic systems in different structural configurations (i.e., alloy, cluster-in-cluster, and core-shell structure) were extensively studied for stabilization of NCs. Among these structures, the core-shell NCs present the most convincing in structure stability across all dimensional regimes. Such unique structure can be developed by depositing the methanol active atoms atop selected core crystallites in monolayers thickness while retaining compressive lattice strain in the shell region.

From heterogeneous crystal growth standpoints, core-shell structure is the simplest platform for lattice strain and composition manipulations at the near surface region in binary NCs. Such structure is normally been developed by properly selecting the identity of core and shell crystallite with precision shell thickness control¹. State-of-the-art studies on core-shell NCs performed the outstanding electrochemical durability in a DMFC test above 10⁵ cycles and CO oxidation activities in fuel reformate system at room temperature²⁻⁴. These experimental results were subsequently confirmed by the density functional

theory (DFT) calculations. Combining experimental and theoretical results the heterogeneous catalytic activity of core-shell NCs is mainly determined by the top layers of shell atoms (about ~4 – 5 Å depth in most cases)^{5, 6}. These implications promised the design of new NCs in frontier green energy devices⁶. However, their electrochemical properties (i.e., activity, selectivity, and stability) remain to be improved for applications at industrial production levels.

To target the industrial application standards, the structure and performance durability of NCs particularly in long-term redox reactions in operational devices are of essential importance. These crucial factors can be improved by increasing the extents of heteroatomic intermix while retaining the densities of surface active site and the lattice strain in the near surface region of NCs. Our previous studies and the literatures demonstrated that the chemical stability of NCs in electrochemical devices (against methanol oxidation reaction “MOR” in a fix voltage anode and fuel cell voltage cycle tests) was strongly depended on the intra-crystallite geometrical confinements. Among the binary systems in different configurations, the core-shell structured NCs present the highest extent of heteroatomic intermix, lattice strain, and the interface conjunction. These features inspiring the electron injection and the heteroatomic intermix (hybridization) and thus significantly enhance the chemical activity (selectivity) and the structural stability (including the anti-protonation corrosion and CO poisoning) on the reaction sites at NCs³.

In this study, the binary NCs comprising 1.5 atomic layers Pt shell and 2.8 nm Ru core was synthesized. To further reinforce

the physiochemical stability of NCs, the gold clusters in sub-nanometer size were intercalated at the inter-facet corner sites atop Pt shell. We demonstrate that these gold clusters trigger the electron injection from core to shell regions. It concentrates the negative charges at corner regions thus ejecting the negative charged anions (CO molecules) from the NCs surface. In this circumstance, the retained current density of Pt shell Ru core NCs is doubled in a long-term MOR at 0.5 volt test after 2 hours by inserting these atomic scaled gold rivets. Such novel structure confinement provides possible strategy for developing the high power and stability module in direct methanol fuel cell (DMFC). Details of the heteroatomic restructure of NCs in relation to the electrochemical performance of MOR will be given in the latter sections. In addition, we will clarify how the structure stability of core-shell structure NCs is further enhanced through the intercalation of the Au clusters at their corner regions. To hit our target, the small angle X-ray scattering (SAXS), high resolution transmission electron microscopy, X-ray absorption, and density functional theory simulation were complimentary employed.

Experiment

The atomic structure of the experimental NCs was controlled by using the sequential designed polyol reduction⁷. The average particle size, size distribution, and the geometry configuration of these NCs were determined by small angle X-ray scattering analysis. The impact of the Au cluster intercalations on the atomic arrangement and the CO sorption manners on NCs were simulated by using ab-initio density function theory (DFT) calculations. The valence band structure was elucidated by UPS spectroscopy. Combining these structure results, the impact of Au cluster intercalations on activity and structure stability of NCs were complimentary resolved at a fix voltage long-term MOR analysis. The details on sample preparation, structure interpretations, and discussions are given in following sections and the electrical supplementary information (ESI).

Materials

The metal precursors (including Hexachloride platinum acid ($\text{H}_2\text{PtCl}_6 \cdot 6\text{H}_2\text{O}$, 99 at%), Hydrogen tetrachloroaurate(III) hydrate (HAuCl_4 , ACS reagent > 49%), and Ruthenium (III) chloride hydrate ($\text{RuCl}_3 \cdot 3\text{H}_2\text{O}$, 99.0%)) and polymer stabilizers (polyvinylpyrrolidone stabilizer (PVP-40, MW ~42,000, 99%) were obtained from Sigma-Aldrich. The H_2SO_4 (99.9%) and HNO_3 (99.9%) were obtained from Sigma-Aldrich. The reaction solvent (ethylene glycol, EG > 99.5%) was obtained from Fluka Co. Inc.

Catalyst Preparation

The $\text{Ru}_{\text{Core}}\text{-Pt}_{\text{Shell}}$ NCs (denoted as PtS/RuC) were synthesized by a two-steps polyol method with the reaction sequences in conformity with the expected atomistic architecture. First, the hcp Ru cores with an average diameter of ~2.5 nm were prepared by reducing 100 mM ruthenium chlorite in ethylene glycol (EG) with the thermal treatments shown in the previous work⁸. Second, the Pt shell in a near monolayer atomic layer was produced basing on a heterogeneous nucleation and growth pathway by a thermal reduction of Pt anions ($\text{H}_2\text{PtCl}_6 \cdot 6\text{H}_2\text{O}$, 99 at%) on the surface of Ru core in a presence of 10 wt% polyvinylpyrrolidone

(PVP) stabilizer in EG at 160°C for 2h. The shell thickness was controlled by adjusting the Pt/Ru ratio to 1.5. The intercalation of gold sub-nanometer clusters at the corner sites of PtS/RuC NCs was conducted by a reducing the gold cations (in an atomic ratio of Au/Pt = 0.1) at the subsequent polyol reactions. In this step, the surface sites of NCs were served as nuclei for catalysing the heterogeneous crystal growth of Au and the resulting NCs is denoted as Au@PtS/RuC.

Catalysts characterizations and methanol oxidation reaction in long-term testing

The microstructure of NCs was elucidated by conventional and high resolution transmission electron microscopy (HRTEM). Nanostructure and crystal structure parameters of NCs were determined by SAXS and XRD at beamlines of **BL-23A** at NSRRC (Taiwan) and **BL-12B2** at Spring-8 (Japan), respectively. The valence band spectrum of the NCs was collected at beamline of **BL-24A1** at NSRRC. The electrochemical stability of the NCs, which was correlated to their surface composition and structures, were determined by fix voltage long-term MOR reaction analysis (CH Instruments Model 600B). The electrochemical cell for CV analysis consisted of a working electrode, an SCE reference electrode, and a 10 mm × 10 mm platinum foil counter electrode. The details for the characterization methods and instrumental parameters are given in ESI.

Density Functional Theory simulations

The theoretical analysis of first-principle calculations and analysis were performed by using Vienna ab initio simulation package (VASP) based on density functional theory (DFT). The Projector augmented wave (PAW) potentials were used to describe the core electrons. Generalized gradient approximation (GGA) in the form of Perdew-Burke-Ernzerhof (PBE) functional is adopted to describe the exchange correlation functional, which is developed for the calculation of surface system. The Pt supercell was simulated by a repeating 6×6 slab model in which 1.5 atomic layers of Pt atoms (packing in (111) facet symmetry), 4-layers of Ru atoms (in (110) facet symmetry) as sub-layer slab, and 5 Au atoms as cluster intercalated at the corner sites. In these calculations, the vacuum region was set into 30 Å in minimizing the potential interferences between top and bottom surfaces on the periodic slabs. In brief, the periodic slab comprises four layer of Ru, one and half layers of Pt atoms, and a vacuum layer of 30 Å; where the CO molecules was allocated at the corner sites of the top surface. The kinetic energy cut-off of 300 eV for the plane wave basis is used. Finally, the cut-off plane wave expansion was taken to be 300 eV and the Monkhorst - Pack mesh of k -points for irreducible Brillouin zone (IBZ) was chosen to be 6×6×1. The structure was optimized until the energy and net force on every atom are smaller than 10^{-5} eV and 0.025 eV Å⁻¹, respectively.

Results and Discussions

Nanostructure of the nanocrystallite

The nanostructure (including the particle shape, average particle size (D_{avg}), surface configurations, and crystal structure)

Cite this: DOI: 10.1039/c0xx00000x

www.rsc.org/xxxxxx

ARTICLE TYPE

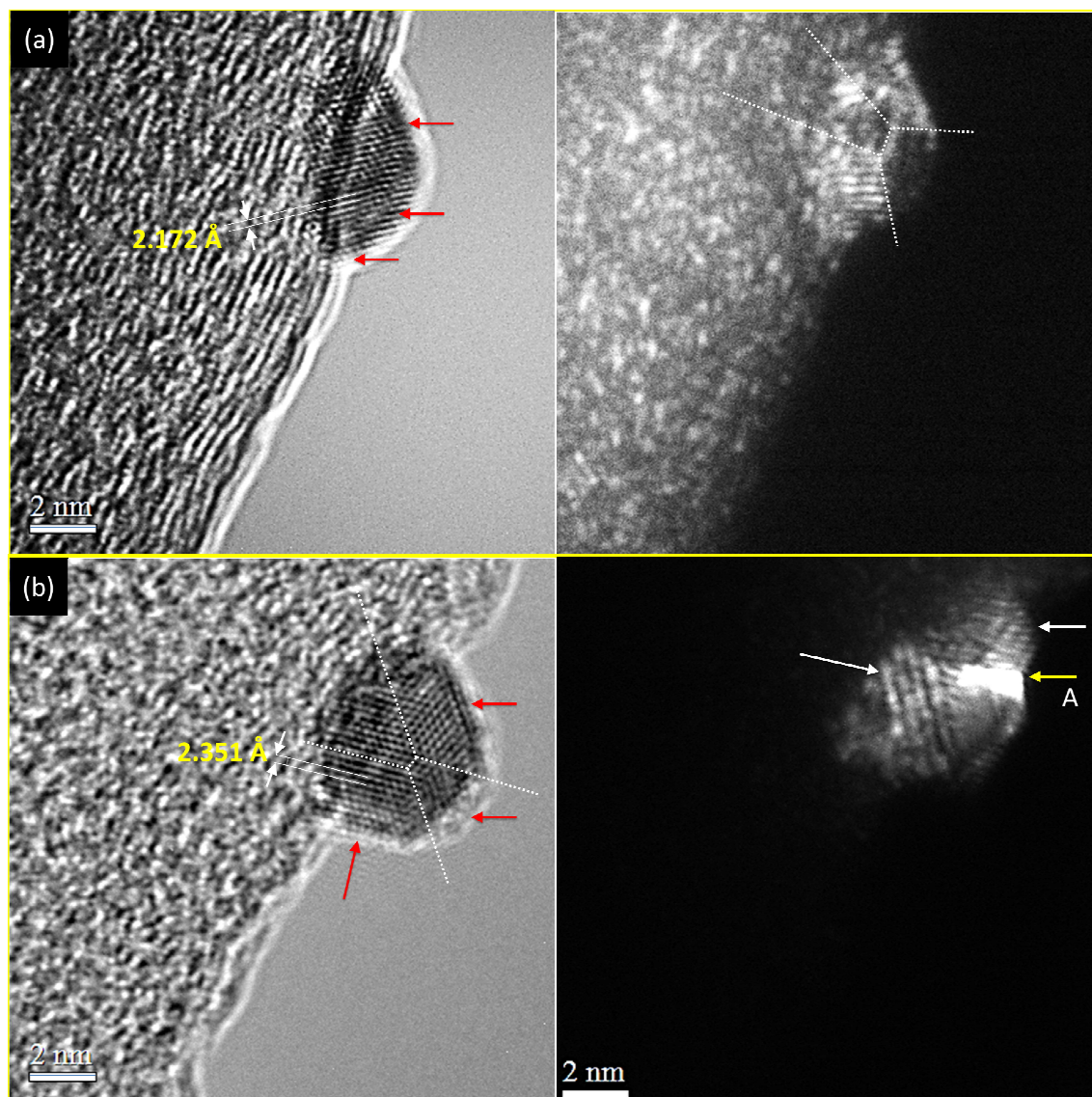


Fig. 1 Bright and dark field high resolution transmission electron microscopy (HRTEM) images of (a) Pt/RuC and (b) Au@Pt/RuC; where NCs were dispersed on glassy carbon grid.

of the NCs and were elucidated by using high resolution transmission electron microscopy (HRTEM). The bright and dark field HRTEM images for the Pt/RuC and Au@Pt/RuC NCs are shown in **Figure 1**. As shown in **Fig. 1a**, the Pt/RuC is grown into multifaceted crystallite with preferential orientation at (111) facets exposing to the surface in different directions (denoted by the arrows in red). These NCs are disk-like in shape which is grown by allocating the Pt atoms atop Ru(0001) facet; where twin boundaries (denoted by the white dashed lines in bright or dark fields images) at inter-facet regions indicate the formation of semi-coherent interfaces. Here, the inter-planar spacing is

15 determined to be 2.172 Å which is compressed by about 3.9% compared to that of Pt (111) facet of metallic Pt (~2.262 Å). Such lattice compression is triggered by allocating the large lattice space crystal (Pt (111) facets) at the small lattice space substrate (Ru (0001) facets). In addition, this lattice compression is applied in the lateral direction at the near surface region. For the case of Au@Pt/RuC (**Fig. 1b**), the lattice space at twin facets is determined to be 2.351 Å. It suggests that Au atoms are possibly grown atop (111) face facets of Pt or at edge sites of Pt/RuC nano disk.⁹ Given that the Au crystal possesses higher surface energy than that of Pt, these Au clusters would tend to grow as

plateaus that truncating the corner sites to form additional (111) facets at the corner sites of PtS/RuC (see **Fig. S1**) via a transmetallation reaction of $2\text{Au}^{3+} + \text{Pt}^{\text{M}} \rightarrow 2\text{Au}^{\text{M}} + \text{Pt}^{6+}$ followed by the reduction of Au^{3+} at the heterogeneous nuclei (Au^{M}) upon interacting with CH_3CHO : radicals^{3, 6, 10, 11}. The formation of Au clusters and the transmetallation induced crystal truncation are further revealed by dark field HRTEM at a tilted angle (**Fig. 1b** in left). As indicated, the prevailing bright spheres (denoted by solid arrows in white) resembling the strong electron refraction atoms in ordered arrangement at (111) atomic packing geometry at different orientations exposing to the NCs surface. The arrow A in yellow denotes the presence of surface stage. This asymmetric crystal shape cannot be formed by the homogeneous crystal growth pathways and thus a direct indication for the growth of external crystal / clusters at the inter-facet corner axes sites.

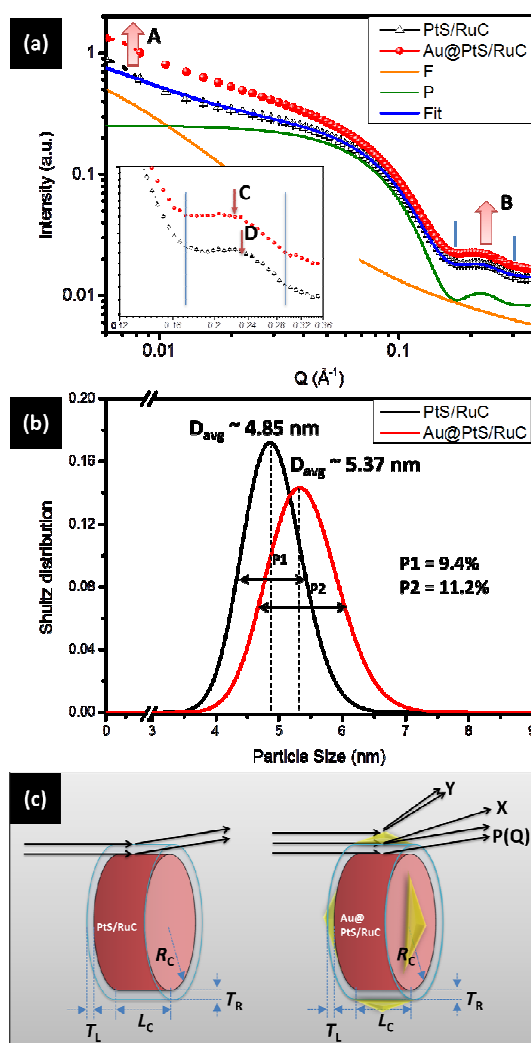


Fig. 2 (a) small angle X-ray scattering spectra, (b) Schulz particle size distribution, and (c) the scattering contributions of the proposed binary structural models for fitting the experiment SAXS spectra.

The results of HRTEM sketch the steric scattering model for refining the structure parameters of core-shell structured NCs (including D_{avg} , Schulz distribution of particle size (P_R), shell thickness (T_S)) in SAXS analysis. In this work, the particle shape and sequences of crystal growth for each component are taken

into account in building these models. The SAXS spectra [$I(Q)$ vs Q] and the corresponding Schulz distributions of particle size are shown in **Fig. 2a** and **2b**, respectively. The features of SAXS spectrum comprise the interferences of incident X-ray photons that scattered between the inter-particle clusters (i.e., the structure factor $F(Q)$ in $Q < 0.07 \text{ \AA}^{-1}$) and intra-particle interfaces of the NPs (the form factor $P(Q)$ in $Q > 0.07 \text{ \AA}^{-1}$). For PtS/RuC, the SAXS spectrum can be described combining the contributions of fractal aggregate and core-shell cylindrical models (see Equation (1) for PtS/RuC and Equation (2) for Au@PtS/RuC).¹²⁻¹⁴

$$I(Q) = A^F S(Q)^F P(Q)^F + A^{\text{CS-C}} S(Q)^{\text{CS-C}} P(Q)^{\text{CS-C}} \quad (1)$$

$$I(Q) = A^{\text{Fclu}} S(Q)^{\text{Fclu}} P(Q)^{\text{Fclu}} + A^{\text{CS-C}} S(Q)^{\text{CS-C}} P(Q)^{\text{CS-C}} \quad (2)$$

In **Equation (1)**, A is the number density of the scattering objects. Both the $S(Q)$ and the $P(Q)$ are the function of the momentum transfer (Q) between incident and scattered X-ray. Q is given by $Q = (4\pi / \lambda) \times \sin(\theta/2)$ in an elastic scattering process; where θ denotes the angle between the incident and the scattered beams at a wavelength of λ . The superscripts F (fractal) and the CS-C (core-shell cylinder) refer to which model the parameters belong to. For the case of Au@PtS/RuC, the incident X-ray will scatter between the Au clusters and at the intra-particle surface (denoted by **arrow X**); where a scattering scheme of the model of Au clusters at core-shell cylinder particle is shown in **Fig. 2c**. The scattered X-ray at Au cluster on the core-shell NPs contributes to the diffusion scattering background (denoted by **arrows Y**); where the inter-particle scattering correlation factors (A^F , $S(Q)^F$, and $P(Q)^F$) are modified into the inter-cluster ones and represented by A^{Fclu} , $S(Q)^{\text{Fclu}}$, and $P(Q)^{\text{Fclu}}$ (see **Equation (2)**). The corresponding fitting curves are shown in **Fig. 2a**. As clearly depicted, for PtS/RuC NCs, the least-square fitting curves of the proposed model fit the SAXS spectrum well (the fitting curves for all samples are given in **Fig. S2**). The broadening and downshift of $F(Q)$ oscillation hump (**from D to C**) elucidate the increasing phase divergence (caused by the X-ray scattering at high roughness surface “**arrow Y**” and the Au-Pt interface, **arrow X**) and the interference cavity length (the distance between inner and outer boundaries of core-shell NCs, T_S) in the presence of Au intercalations. The geometrical scattering inferences of Au clusters were further revealed by comparing the P_R and D_{avg} of the two NCs. As shown in **Fig. 2b**, the D_{avg} of PtS/RuC is determined to be 4.85 nm with a P_R of 9.4% suggesting the convinced particle size distributions and T_S uniformity. For Au@PtS/RuC the D_{avg} is determined to be 5.37 nm which is about 2.0 atomic layers thicker than that of PtS/RuC. Considering to the input Au/Pt ratio, this value seems controversial, however, can be explained by the model of heterogeneous thin-film growth with mild layer-plus-island (Stranski-Krastanov “SK” mode) at the inter-facet corner sites. This phenomenon is consistently elucidated by the scattering model in **Fig. 2c**. In this case, the scattering X-ray will be diffused by the discontinued interfaces between Au clusters and thus resulting in the P_R expansion to 11.2%.

Table 1. The structure parameters of PtS/RuC and Au@PtS/RuC NCs determined by fitting the corresponding SAXS spectra with binary models comprising polydispersed core-shell cylinder and fractal components

NCs ^a	D_{avg} (nm)	R_C (nm)	L_C (nm)	T_R (nm)	T_L (nm)	P_R (%)	D^{clu} (nm)
PtS/RuC	4.85	1.54	2.45	0.83	0.49	9.4	
Au@PtS/RuC	5.37	1.48	2.83	0.75	0.51	11.2	0.5

^a D_{avg} , R_C , L_C , T_R , T_L , P_R , and D^{clu} denote the average particle size, the radius in radial side, the length at face side, the shell thickness at radial side, the shell thickness at face side, the Schulz distribution of particle size, and the diameter of cluster, respectively..

The impacts of Au clusters on structure parameters of these core-shell cylinder NCs (including the mean core radius “ R_C ”, core length “ L_C ”, and the corresponding shell crystal thicknesses of T_R and T_L atop their surface, respectively) were quantitatively derived by model analysis and the results are summarized in **Table 1**. As depicted, the PtS/RuC comprises thin shell crystal of $T_R = 0.83$ nm and $T_C = 0.49$ nm at the face (in a diameter ($R_C \times 2$) of 3.08 nm) and radial (in a L_C of 2.45 nm) axes, respectively. A slight increase of L_C accompany with reducing of T_R is found on Au@PtS/RuC. This character echo the preferential spontaneous transmetalation at the radial surface (where prevailing with high surface defect density) compared to the face surface on the nano-disk NCs. Hence, the defects at the zone axes of the facets (i.e., corners) act as the nucleation sites for allocating the Au clusters (in a size of $\sim 0.5 - 0.6$ nm)^{10, 15}. As complimentary revealed by HRTEM, the growth of these discrete Au clusters truncate the PtS/RuC corners and creating the small close packing facets.

25 Valence band structures of the nanocrystallite

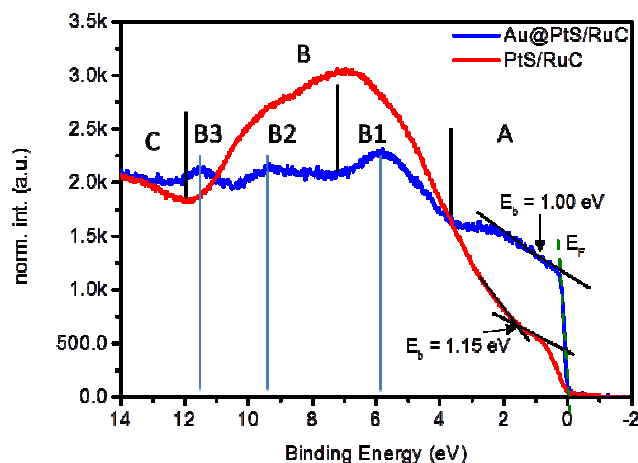


Fig. 3 Valence band spectra of PtS/RuC and Au@PtS/RuC NCs

Valence band electrons are the direct mediators in charging of the catalytic interactions (i.e., the chemisorption/ejection of reagent/product molecules at/from active reaction sites) at the NCs. Its distributions are dominated by the heteroatomic intermix, the surface atomic arrangements, defect density, and the types of heterojunction at the near surface regions. From heterogeneous catalysis standpoint, the surface defects (for instance the kinks / steps and corner sites) are dilemma on the performance of NCs. On the bright side, these defects prevailing with dangling bonds are high surface free energy sites that enabling the redox

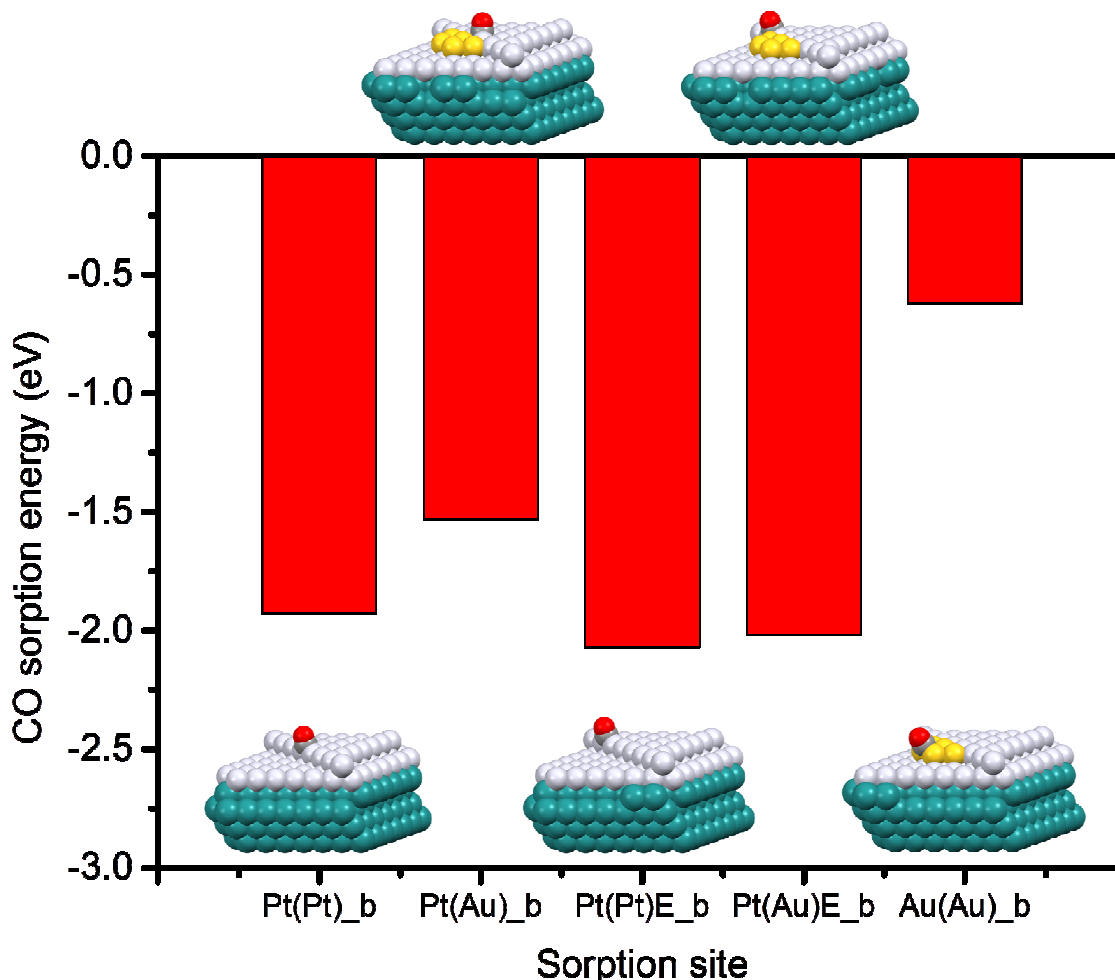
reactions in low activation energy pathways. However, on the dark side, these regions shorting of interatomic bonding support that are both chemically (tend to be poisoned by chemisorption molecules) and mechanically instable (tend to relocate into clusters in reducing the surface free energy). The intercalation of Au clusters adds the localized heterojunction at the PtS/RuC. It not only reinforces the defect sites from restructure but also raises a strong negative charge dipole field for shielding the neighbouring Pt atoms from chemical poisoning. These proposed shielding effects are consistently elucidated by the valence band photoemission spectroscopy (VB). The VB spectra of PtS/RuC and Au@PtS/RuC are compared in **Fig. 3**. As clearly revealed, the VB of NCs comprises several regions: (A) a steep ranging from 0.00 to 0.75 eV, a hillside with a reflection point at 1.15 eV (i.e., the surface binding energy, E_b), and a second climb with high slope till 3.41 eV; (B) a broad band across 3.41 to 11.78 eV (centred at ~ 6.9 eV); (C) a valley centred at 12.3 eV. In comparing with VB spectra of Ru and Pt NCs, since substantial modifications on the VB features are found, the obtained spectrum should not be regarded as the sum of their individual contributions. Instead, it resembles the hybridization of sublayer crystal (in our study, the Ru core NCs) at the VB structures of outer shell crystal (Pt). Given that the intensity of the VB below the Fermi level is normalized to be same, the substantial attenuated intensity (**region A**) indicates the prevailing empty states (a significantly decreased density of states, DOS) at the outmost band. Such open valence states are caused by the heterojunction controlled charge relocation (a local charge injection) from Pt to the sublayer core crystal and the oxygen chemisorption^{4, 9}. A broad hump with strong intensity in the **region B** could be attributed mainly to the valence band compression in combination with certain extends of oxidation at the Pt crystal. These valence band structures, basing on the DFT predictions in the literatures, tend to accept the electrons from the chemisorption molecules, thus, facilitate the initial MOR current of PtS/RuC (results are given in the later sections). Region C resembles the near core level photoemission signals; where dramatic increased emission intensity is found at the binding energy above 11.8 eV (the extended VB spectra are shown in **Fig. S3**). Compared to that of PtS/RuC, a quantum leap of photoemission intensity is found in the **region A**. Such novel character resembles the preservation of valence charge at particle surface by the localized heterojunction around the Au clusters atop Pt shell crystallite. As elucidated by our DFT simulations (**Fig. S4 and Table S1**), these negative charge domains (Au intercalations) together with the sub-level charge injection band weaken the chemisorption of anion species (oxygen in our case) and thus protect the particle surface from oxidation. Such weakening coincides to the reduced surface E_b ($\sim 0.95 - 1.00$ eV) compared to that of PtS/RuC. In the high binding energy region (**region B**), the band width is expanded to 12.3 eV and splitting into **B1**, **B2**, and **B3** centred at 6.1, 9.3, and 11.6 eV, respectively. The centres of these distinct band features coincide to that of metallic Pt crystallite at varies facets. In addition, compared to the Pt metallic bands with surface oxidation (**Fig. S3**), the energy upshift and shape modifications on these splitting bands again proving the formation of anti-oxidation shielding of Au clusters at Pt shell. With such shielding, the protonation corrosion, surface

oxidation, and CO poisoning resistances of Pt/RuC will be substantially improved. These hypotheses are proved by combining the results of DFT simulations (Fig. S4), X-ray absorption spectroscopy analysis (Fig. S5), and long-term MOR test.

Au clusters shielding the CO chemisorption

Basing on heterogeneous crystal growth theory and the results

of structural analyses, we can note that the Au clusters tend to intercalate at the inter-facet corners of Pt/RuC. These clusters protect the most active sites from direct interacting to the carbonaceous retentions (i.e., CHO and CO ligands) and thus substantially enhancing the MOR activity of NCs in long-term operation.



15 Fig. 4 DFT simulation CO sorption model on 1.5 MLs of Pt atoms atop Ru (0001) facet with and without Au clusters at the kink region with the corresponding sorption energies.

Such hypothesis was proved by via ab-initio DFT simulation. In our work, five close packed Au atoms were allocated at the kink region as cluster that intercalate at Pt atop Ru heterojunction slab (one and half layers Pt atoms atop four sublayers Ru (110) facet) for simulating the shielding effects on the CO bonding energy at PtS/RuC NCs. On the PtS/RuC substrate, these Au atoms (yellow spheres) are close packed at the kink region of Pt shell (Fig. S4). It is important to note that the heteroatomic bond length (Table S2) at the interface (i.e., Pt1-Au1 and Pt2-Au2) is determined to be 2.852 +/- 0.08 Å. This value is ~0.07 Å longer than that of homoatomic Pt-Pt bond distance (~2.779 +/- 0.06 Å) which is an indication for the preferential clustering of Au atoms by minimizing the surface free energy⁶. Consequently, a local lattice compression at Pt shell adjacent to Au cluster by the lattice mismatch is expectable. As consistently revealed by Pt and Au 4f core level XPS (Fig. S6 and Table S3) and VB spectra (Fig. 3),

this strain and electronegative dipole extract the electrons from Pt shell to Au cluster. It builds a negative charge field and thus protects the Pt shell from oxidation and CO poisoning at the Au@PtS/RuC surface. The DFT simulation results consistently elucidate these electronic relocation impacts on chemisorption manners of the charge demanding sorbates (i.e., O ligand and CO molecules) at NCs. The simulation models (comprising CO molecule on bridge sites at top layer and edge of Pt shell and bridge site on Au cluster) with the sorption energy are shown in Fig. 4 (structure parameters are summarized in Table S2). As depicted, the sorption energy of CO at bottom bridge sites (where CO is allocated at the surface of one monolayer Pt atop Ru(0001) facet) is determined to be ~1.13 eV which showing consistent result with that was done in literatures^{3, 5}. The sorption energies on bridge sites at top layer (with 1.5 monolayers Pt atop Ru(0001) and at edge are found higher than expected (should be the value

between 1.13 (1.0 layer) to 1.33 eV (2.0 layer)). Such controversial could be rationalized by the formation of strong chemisorption that eliminating the defect density in the consideration of surface energy minimization. In this circumstance, the CO sorption energy at the edge Pt-Pt bridge sites (**Pt(Pt)E_b**) is ~ 0.14 eV larger than that at top layer sites (**Pt(Pt)_b** -1.97 eV) resembling the CO sorption preference in PtS/RuC. In the case of Au@PtS/RuC, the similar preference is expectable. However, compared to **Pt(Pt)E_b**, it is surprising to note that the sorption energy is substantially increased by ~ 0.41 eV (-1.53 eV) at the Pt-Pt bridge sites neighbouring to Au clusters (**Pt(Au)_b**) and an even higher energy (-0.62 eV) is found on the Au-Au bridge sites at Au cluster (**Au(Au)_b**). These results are convincing implications for the reinforcements of chemical stabilities on PtS/RuC by the Au intercalations during the MOR in long-term test. Combining the results of band structure simulation and VB spectra, such CO shielding effects could be attributed to the electron extraction from Ru core and Pt shell to Au clusters via the localized strain field at the heterojunction. In this case, the Au@PtS/RuC possesses a charge prevailing domains for ejecting the anion ligands (OH⁻ or O²⁻) or electronegative molecules (e.g., CO) from its surface.

Catalyst MOR stability

The stability of NCs was investigated by chronoamperometric analysis (typically named as AC analysis) at long-term MOR.

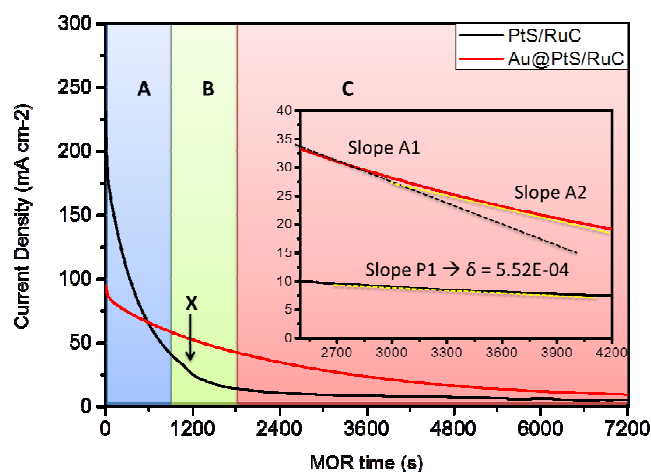


Fig. 5 The electrochemical spectra of the two experimental NCs for long-term MOR reaction (inset shows line fitting for the current drop).

The current-to-time curves for the MWCNT supported PtS/RuC and Au@PtS/RuC NCs against MOR at a fixed applied voltage (0.5 volt vs. SCE) are shown in **Fig. 5**. Three current regions A, B, and C are found on the AC curve corresponding to the changes of current density by the surface atomic restructure, the redox electrochemical kinetic unbalance, and the CO poisoning, respectively. As illustrated, the initial current density of PtS/RuC NCs is determined to be ~ 225 mA cm⁻² mg⁻¹, which is $\sim 150\%$ higher than that of Au@PtS/RuC (~ 92 mA cm⁻² mg⁻¹). Compared to PtS/RuC, the electrochemical surface area of Au@PtS/RuC is reduced by only $\sim 11\%$. Hence, such abnormal current drop could mainly be attributed to the suppression of methanol chemisorption kinetics by the presence of negative charge field around Au intercalations instead of geometric capping effects. In

region A, the MOR activity of PtS/RuC NCs was exponentially decayed by 78% in the first 15 min. The high current drop rate can be rationalized by the competition between hydroxide (OH⁻) ligands and the reactants (methanol in this case). These OH ligands form the electrostatic double layer (EDL). It hinders the subsequent chemisorption of methanol and thus suppresses the MOR current of PtS/RuC^{16, 17}. However, the current drop in region A is reduced to $\sim 30\%$ on the AC of Au@PtS/RuC. It reveals the shielding effects at the most reactive corner sites from OH ligand by the Au clusters. Once the competition between sorption kinetics of MeOH molecule and OH ligands meets a thermodynamic metastable balance (denoted by arrows X for PtS/RuC), the subsequent stability of reaction activity (current density in **region B**) are dominated by the atomic structure on the NCs. After reaction time passed the X node, an inversion point on AC current vibration is found implying the certain extent of atomic restructure by the protonation corrosion in PtS/RuC. This corrosion is facilitated by the surface oxidation at Pt corner site and is inevitable without protecting the structure of NCs. On the other hand, no inversion point is found in region B suggesting that the protonation corrosion is substantially suppressed by the intercalation of Au cluster at Au@PtS/RuC.

The CO tolerance capability of the NCs can be depicted by the rate of current drop (δ) in **region C** on the long-term MOR AC curves (see inset of **Fig. 5**) in a numerical representation¹⁸:

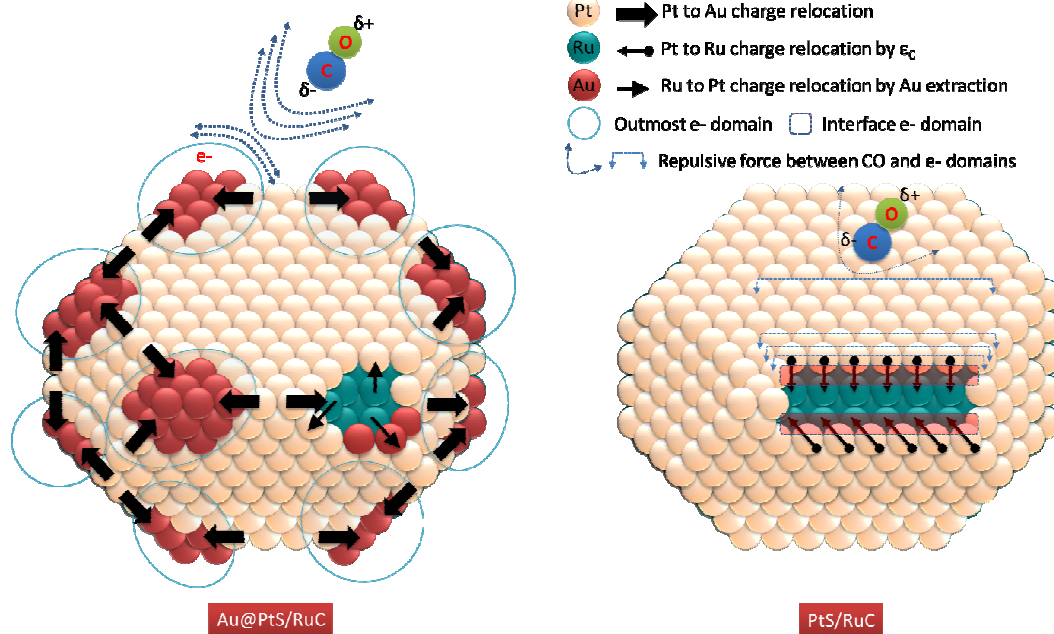
$$\delta = -\frac{100}{I_0} \times \left(\frac{dI}{dt} \right) (\% s^{-1}) \quad (3)$$

where I_0 and dI/dt refer to the initial current density and the rate of current drop in a short reaction period. Accordingly, the $\delta(\text{PtS/RuC})$ is determined to be $-5.52\text{E}-04$. It is interesting to note that the current drop rate have not stabled to a constant value on Au@PtS/RuC (denoted by the different values of slope A1 and slope A2 at the beginning and end point of AC in inset). As consistently elucidated by DFT simulations, this feature implies that the chemisorption kinetics between poisoning ligands (i.e., OH and CO) and the reactant (MeOH) remain in debating in this region since the most active CO sorption sites (edge bridge sites) were protected by the less CO poisoned Au atoms. Such unique character rationalized the superior retention current (2.5-folds) of Au@PtS/RuC compared to that of PtS/RuC in the MOR for 2 hours.

Our previous studies had demonstrated that the lattice compression at Pt shell crystallite triggers the electron injection from Pt to sublayer core crystal. As consistently revealed by theoretical implications and VB spectrum analysis in literatures, this charge relocation build a negative charge riched domain at the interface (**Scheme 1**). It weakens the chemisorption bond of electronegative sorbates and thus improves the chemical stability of NCs in electrochemical redox applications (for example, CO oxidation, MOR, and DMFC *et al.*). In this work, we demonstrate that such electron injection could be further enhanced and localized by the Au clusters at inter-facet corner (**Scheme 1**). These Au clusters triggers a strong local compression strain at Pt shell and extract certain electrons from the neighbouring Pt shell crystal and even from the core crystal. This charge relocation pathway seems disobeying the well-studied practices of

enhancing the CO oxidation activity by applying the lattice

compression Pt shell crystal.



Scheme 1 The proposed atomic packing structure with corresponding electron relocation pathways on Ru core-Pt shell NCs w/ and w/o intercalating by sub-nanometer Au clusters. This Au clusters extract the valence charge from Pt and Ru crystallites to form a negative charge shielding that protecting the core-shell NCs from passivating by CO molecules.

However, it generates a localized electron charge field that shining even stronger repulsing force to weaken the bonding of electronegative molecules (e.g., CO chemisorption) atop the Au cluster and the neighbouring reaction sites. These electrochemical properties / hypothesis are consistently explained by combining results the VB spectra analysis and ab-initio DFT simulation^{19,20}. Accordingly, the external strain extracts the electrons from Ru to Pt to the outmost band of NCs. It shift-up the d-band centre of the core-shell NCs⁹. Both of these features are consistent to the results of AC analysis again promising the outstanding CO tolerance and electrochemical stability of Au@PtS/RuC.

Conclusions

A novel polyol redox method with sequence design was employed for intercalating the Au clusters at the inter-facet regions of Ru core – Pt shell NCs. Our systematic structural characterizations in combination with the theoretical simulations demonstrate that these gold clusters would tend to allocate at the inter-facet corner sites of the core-shell NCs. Such heterogeneous crystal growth is initiated by the redox transmellation nucleation followed by the thermal reduction of Au ions into metallic crystal. These clusters truncate the interfaced corners (reduce the surface defects) and grow into close packed facets in small area. In this circumstance, the methanol electrooxidation stability of the NCs was substantially improved. Combining DFT simulations and spectroscopy analyses, such stabilization was originated by the prevention of surface oxidation and the weakening of CO poisoning at the Pt sites adjacent to the Au clusters. The former suppresses the oxidation assisted protonation corrosion (i.e., reinforces the atomic structure) and the later prolongs the MOR activity (preserve the reaction site “Pt” from being occupied by

the OH ligand or CO molecules) of Pt atoms at the NCs. Both the two pathways are triggered by the localized strain field at the heterojunction between Au and Pt shell. The heterojunction Au crystal covers the in-plant dangling bond at and stabilizes the Pt atoms at the kink. The local strain field in combination with the negativity dipole extracts the electron from core and Pt shell to the Au clusters. Such charge extraction leaps the DOS on the outmost band of NCs. It forms the negative fields to eject the high electronegative ligand/molecules around Au cluster and thus enhances the MOR stability of NCs. Most importantly, our results demonstrate the robust surface modification technique (with fundamental understandings) for developing high durability catalysts for long-term electrochemical reactions.

Acknowledgements

The authors would like to thank the staff of National Synchrotron Radiation Research Center (NSRRC), Hsinchu, Taiwan for the help in various synchrotron-based measurements. We appreciate the help from National Center for High-Performance Computing (NCHC) of Taiwan for providing computational support. T.-Y. Chen acknowledges the funding support from research projects of the National Tsing Hua University, Taiwan (N103K30211 and 103N1200K3) and the Ministry of Science and Technology, Taiwan (MOST 103-2112-M-007 -022 -MY3).

Notes and references

^a Department of Engineering and System Science, National Tsing Hua University, Hsinchu 30013, Taiwan Fax: +886 3 5728445; Tel: +886 3 5742671; E-mail: chencaeser@gmail.com

^b Institute of Nuclear Engineering and Science, Hsinchu 30013, Taiwan Fax: +886 3 5728445; Tel: +886 3 5742671; E-mail: chencaeser@gmail.com

^c Department of Physics, National Tsing Hua University, Hsinchu 30013, Taiwan; E-mail: dengsunglin@gmail.com

^d Department of Environmental Science and Engineering, Tunghai University, Taichung 40704, Taiwan; E-mail: yliu@thu.edu.tw

^e National Synchrotron Radiation Research Center, Hsinchu 30013, Taiwan

† Electronic Supplementary Information (ESI) available: The DFT simulation, XAS, XPS, and TEM results are enclosed. See DOI: 10.1039/b000000x/

- 10 1. S. Goto, S. Hosoi, R. Arai, S. Tanaka, M. Umeda, M. Yoshimoto and Y. Kudo, *The Journal of Physical Chemistry C*, 2014, **118**, 2634–2640.
2. K. Sasaki, H. Naohara, Y. Cai, Y. M. Chio, P. Liu, M. B. Vukmirovic, J. X. Wang and R. R. Adzic, *Angewandte Chemie International Edition*, 2010, **49**, 8602-8607.
- 15 3. S. Alayoglu, A. U. Nilekar, M. Mavrikakis and B. Eichhorn, *Nature Materials*, 2008, **7**, 333-338.
4. P. Strasser, S. Koh, T. Anniyev, J. Greeley, K. More, C. Yu, Z. Liu, S. Kaya, D. Nordlund, H. Ogasawara, M. F. Toney and A. Nilsson, *Nature Chemistry*, 2010, **2**, 454–460.
- 20 5. A. Schlapka, M. Lischka, A. Gross, U. Kasberger and P. Jakob, *Physical Review Letters*, 2003, **91**, 016101.
6. T. Bligaard and J. K. Nørskov, *Electrochimica Acta*, 2007, **52**, 5512-5516.
- 25 7. Y. Sun and Y. Xia, *Science*, 2002, **298**, 2176-2179.
8. T.-Y. Chen, T.-L. Lin, T.-J. M. Luo, Y. Chio and J.-F. Lee, *ChemPhysChem*, 2010, **11**, 2383-2392.
9. R. R. Adzic, J. Zhang, K. Sasaki, M. B. Vukmirovic, M. Shao, J. X. Wang, A. U. Nilekar, M. Mavrikakis, J. A. Valerio and F. Uribe, *Topics in Catalysis*, 2007, **46**, 249-262.
- 30 10. S. Alayoglu and B. Eichhorn, *Journal of the American Chemical Society*, 2008, **130**, 17479-17486.
11. T.-Y. Chen, Y.-T. Liu, H.-S. Chen, K.-W. Wang, C.-T. Yang, T.-J. M. Luo, C.-H. Lee and T.-L. Lin, *CrystEngComm*, 2013, **15**, 3932-3942.
- 35 12. J. Teixeira, *Journal of Applied Crystallography*, 1988, **21**, 781-785.
13. A. Guinier and G. Fournet, *Small-Angle Scattering of X-Rays*, John Wiley and Sons, New York, 1955.
14. J. Wagner, *Journal of Applied Crystallography*, 2004, **37**, 750-756.
- 40 15. J. Greeley and M. Mavrikakis, *Nature Materials*, 2004, **3**, 810-815.
16. C.-C. Hu and K.-Y. Liu, *Electrochimica Acta* 1999, **44** 2727-2738.
17. C.-C. Hu and K.-Y. Liu, *Electrochimica Acta* 2000, **45** 3063-3068.
18. J. Jiang and A. Kucernak, *J. Electroanal. Chem.*, 2003, **543**, 187-199.
19. J.-J. Wang, Y.-T. Liu, I.-L. Chen, Y.-W. Yang, T.-K. Yeh, C.-H. Lee, C.-C. Hu, T.-C. Wen, T.-Y. Chen and T.-L. Lin, *The Journal of Physical Chemistry C*, 2014, **118**, 2253-2262.
- 45 20. J. Ma, A. Habrioux, C. Morais, A. Lewera, W. Vogel, Y. Verde-Gómez, G. Ramos-Sanchez, P. B. Balbuena and N. Alonso-Vante, *ACS Catal.*, 2013, **3**, 1940-1950.

50